Chinese Chemical Letters 33 (2022) 803–806

Contents lists available at ScienceDirect

Chinese Chemical Letters

journal homepage: www.elsevier.com/locate/cclet

Ni nanoparticles encapsulated within H-type ZSM-5 crystals for upgrading palmitic acid to diesel-like fuels

Yanchun Shi[a], Chen Gao[a], Enhui Xing[b], Jimei Zhang[a], Feng Duan[a], He Zhao[a], Yongbing Xie[a,*]

[a] CAS Key Laboratory of Green Process and Engineering, Institute of Process Engineering, Chinese Academy of Sciences, Beijing 100190, China
[b] State Key Laboratory of Catalytic Materials and Reaction Engineering, Research Institute of Petroleum Processing, Sinopec, Beijing 100083, China

ARTICLE INFO

Article history:
Received 18 May 2021
Revised 17 June 2021
Accepted 29 June 2021
Available online 6 July 2021

Keywords:
Post-encapsulation
Ni@HZSM-5
Ni nanoparticles
Palmitic acid
Hydrodeoxygenation
Hydrocarbons

ABSTRACT

Meso-Ni@HZSM-5 bi-functional catalysts were successfully post-encapsulated with about 3–7 nm Ni nanoparticles within HZSM-5 crystals, which exhibited significantly efficient conversion activity (67.4 g[palmitic acid] g[Ni]$^{-1}$ h^{-1}) of palmitic acid and 100% selectivity of hydrocarbons with the outstanding stability during recycling application, compared to the impregnated Ni/HZSM-5 catalyst (14.0 g[palmitic acid] g[Ni]$^{-1}$ h^{-1}).

The increasingly environmental requirements and the dwindling fossil resources have highly encouraged researchers to develop renewable and sustainable energy resources, such as waste oils and fats, vegetable oils, microalgae oils, *etc.* [1,2]. These oleaginous feedstocks generally consist of C_{16}–C_{20} triglycerides and fatty acids (palmitic and stearic acids as main components) with high oxygen contents (10–40 wt%), which lead to the low energy density, the inferior chemical, the inferior thermal stability and so on. Catalytic deoxygenation is considered as the necessary and efficient method for producing high quality biodiesel-like fuels, and three deoxygenation routes are summarized in Scheme S1 (Supporting information) with C_{15}–C_{18} *n*-alkanes as main products as follows: decarboxylation (DCX) (route 1 - DCX: R-COOH → R-H + CO_2), hydro-decarbonylation (HDC) (route 2 - HDC: R-COOH + H_2 → R-H + CO + H_2O) and hydrodeoxygenation (HDO) (route 3 - HDO: R-COOH + $3H_2$ → R-CH_3 + $2H_2O$) [3-6]. The design of effective and stable catalysts is the challenge to determine the deoxygenation performance. Impregnation and ion-exchange methods usually lead to the almost un-restriction of metal leaching, migration and aggregation supports, which are deactivated quickly during recycle runs and regeneration, like Ni/HZSM-5 and Ni/HBeta bifunctional catalysts [7,8]. Recently, encapsulation of metal within zeolites has been reported as the absolutely effective method to synthesize high activity and stability catalysts in many publications [9-11]. Therefore, in this paper, we primarily attempted to encapsulate Ni nanoparticles within H-type ZSM-5 crystals (Ni@HZP-5) *via* the post-encapsulation method derived from the identical parent zeolite (HZ-5-80), which produced a series of meso-Ni@HZSM-5 bi-functional catalysts with similar morphology and further upgraded palmitic acid (PA, as model compound). The detailed information for catalysts synthesis, characterization and catalytic performance was provided in Supporting information.

Physicochemical property of Ni@HZP-5: All Ni@HZP-5 bifunctional were post-encapsulated without/with Al addition to produce the Si/Al gradient descent from 80 to 45 and 30. Larger surface areas and volumes of 4Ni@HZP-5-n and 2Ni@HZP-5-n were obtained (n = 80, 45 or 30, Table S1 in Supporting information) than compared to impregnated 4Ni/HZ-5-80, which were obvious hysteresis loops of the adsorption-desorption curves (Fig. S1A for 4Ni@HZP-5-n and Fig. S1B for 2Ni@HZP-5-n in Supporting information) to suggest the formation of mesopores. The distribution of pore diameters was centered at 3.8 nm based upon Barrett-Joiner-Halenda (BJH) curves (Fig. S1C for 4Ni@HZP-5-n and Fig. S1D for 2Ni@HZP-5-n in Supporting information). As shown in Fig. S2 (Supporting information), all Ni@HZP-5 showed similar diffraction peaks like parent zeolite HZ-5 with well crystallinity in Figs. S2A and B, without any new diffraction peaks with 2θ = 44° and 52° for Ni [111] and Ni [200] planes (4Ni/HZ-5-80, Figs. S2A

* Corresponding author.
E-mail address: ybxie@ipe.ac.cn (Y. Xie).

https://doi.org/10.1016/j.cclet.2021.06.086
1001-8417/

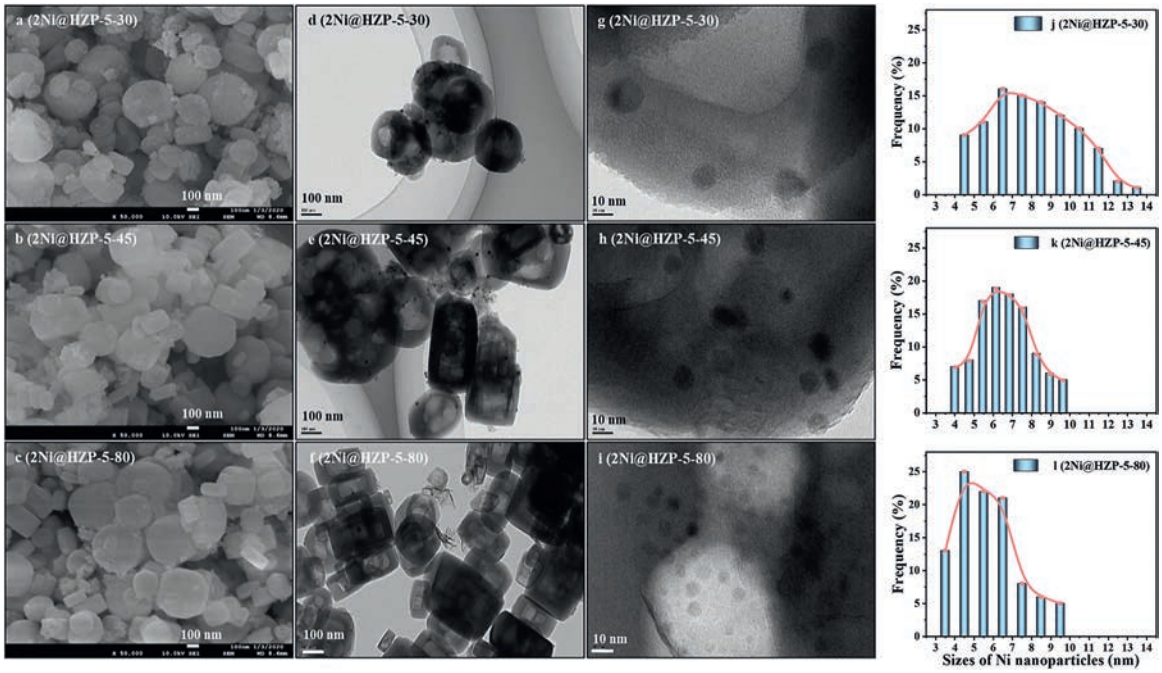

Fig. 1. SEM images, TEM images and Ni size distribution of bi-functional catalysts: (a, d, g, j) 2Ni@HZP-5-30, (b, e, h, k) 2Ni@HZP-5-45 and (c, f, i, l) 2Ni @HZP-5-80.

and B) [7,8], which may indicate the small Ni sizes and the uniform dispersion of Ni nanoparticles within HZP-5 crystals. Additionally, more acid sites particularly for medium/strong acid cites were obtained for 4Ni@HZP-5-n (Fig. S2C) and 2Ni@HZP-5-n (Fig. S2D) than those of 4Ni/HZ-5-80. On the one hand, it could be seen that the lower Si/Al ratios, the number of acid sites were increased with similar Ni contents; on the other hand, the more Ni contents could improve the strong acid sites with similar Si/Al ratios.

The chemical states of Ni species over Ni@HZP-5 were analyzed in Fig. S3 (Supporting information) by X-ray photoelectron spectroscopy (XPS). The fitting peaks of Ni 2p region could be divided into two/three peaks about Ni^0 (854.7–856.1 eV for Ni $2p_{3/2}$ and 872.5–874.3 eV for Ni $2p_{1/2}$), Ni^{2+} (857.1–860.8 eV for Ni $2p_{3/2}$ and 875.0–878.5 eV for Ni $2p_{1/2}$) and/or satellite peaks (862.2–864.0 eV for Ni $2p_{3/2}$ and 880.8–882.5 eV for Ni $2p_{1/2}$) [12-14]. Binding energies of Ni^0 for all Ni@HZP-5 were shifted about 1.7–3.1 eV for Ni $2p_{3/2}$ and 2.5–4.3 eV for Ni $2p_{1/2}$ toward higher values, compared to 853 eV for Ni $2p_{3/2}$ and 870 eV for Ni $2p_{1/2}$ of nickel metal [12], which may be ascribed to both the quantum size effect of Ni^0 nanoparticles and the electronic properties of zeolite matrix [13,14]. The similar phenomenon has also been reported by zeolites encapsulation Pt [14] and Ni [15]. On the one hand, the more Ni encapsulation, the higher values of Ni^0 binding energies were observed between 2Ni@HZP-5-n and 4Ni@HZP-5-n at similar Si/Al ratios; on the other hand, the higher Si/Al ratios, the more Ni^{2+} species were reduced to form Ni^0 centers especially for 4Ni@HZP-5-n (Figs. S3d-f). Significantly, there was no detection of Ni^{2+} species for 2Ni@HZP-5-80 (Fig. S3c), which indicated that all Ni^{2+} species were reduced to Ni^0.

Fig. 1 gives scanning electron microscopy (SEM) images, transmission electron microscope (TEM) images and Ni size distribution of 2Ni@HZP-5-n (n = 30, 45 or 80). There was no obvious difference in the morphology of 2Ni@HZP-5-30 (Fig. 1a), 2Ni@HZP-5-45 (Fig. 1b) and 2Ni@HZP-5-80 (Fig. 1c), which may be ascribed to the identical parent zeolite. While there existed significant differences in these three 2Ni@HZP-5-n (n = 30, 45 or 80) with the increase of Si/Al ratios by TEM. Firstly, many mesopores were absolutely observed (Figs. 1d–i), which was in agreement with BET analysis (Fig. S1B). Secondly, more and smaller Ni nanoparticles were exhibited by the increase of Si/Al ratios, with distributed mainly in 4–11 nm for 2Ni@HZP-5-30, 5–8 nm for 2Ni@HZP-5-45 and 3–7 nm for 2Ni@HZP-5-80. Similar results of 4Ni@HZP-5-n (n = 30, 45 or 80) were obtained in Fig. S4 (Supporting information), which were different in those of 4Ni/HZ-5-80 (Fig. S5 in Supporting information). Thus, the less Ni contents and the higher Si/Al ratios usually led to the weaker interaction between Ni and Al, which was not only beneficial for the reduction of Ni^{2+} to Ni^0 (Fig. S3), but also for the formation of smaller Ni nanoparticles. The observation of small Ni nanoparticles especially for 2Ni@HZP-5-80 with 3–7 nm, was also accordance with in X-ray diffraction (XRD) results with no obvious diffraction peaks of Ni species *via* the post-encapsulation method.

Hydrodeoxygenation performances: As shown in Fig. 2, Ni@HZP-5 bi-functional catalysts catalyzed PA at identical reaction conditions (260 °C and 4.0 MPa H_2) as function of reaction time. With prolonging reaction time (Fig. 2A), PA conversion increased to demonstrate that enough reaction time would bring PA into contact with active centers. At 240 min, 2Ni@HZP-5-80 exhibited higher conversion (99.7%, Fig. 2A-e) than 2Ni@HZP-5-45 (93.0%, Fig. 2A-c) and 2Ni@HZP-5-30 (84.3%, Fig. 2A-a, with error bar); the similar results were obtained over 4Ni@HZP-5-80 (91.4%, Fig. 2A-f), 4Ni@HZP-5-45 (69.9%, Fig. 2A-d) and 4Ni@HZP-5-30 (57.5%, Fig. 2A-b). The higher conversion was obtained over 2Ni@HZP-5-n bi-functional catalysts with low Ni contents than those over 4Ni@HZP-5-n at similar Si/Al ratios, especially for 2Ni@HZP-5-80. To further evaluate the activity, turn over frequency (TOF, g[PA] $g[Ni]^{-1}$ h^{-1}) of Ni@HZP-5 bi-functional catalysts were calculated at initial 1 h in Table 1 [16], as comparison of impregnated 4Ni/HZ-5-80. The corresponding TOF were 33.8 g[PA] $g[Ni]^{-1}$ h^{-1} for 4Ni@HZP-5-80, 32.1 g[PA] $g[Ni]^{-1}$ h^{-1} for 4Ni@HZP-5-45, 29.4 g[PA] $g[Ni]^{-1}$ h^{-1} for 4Ni@HZP-5-30, 67.4 g[PA] $g[Ni]^{-1}$ h^{-1} for 2Ni@HZP-5-80, 45.0 g[PA] $g[Ni]^{-1}$ h^{-1} for 2Ni@HZP-5-45 and 31.6 g[PA] $g[Ni]^{-1}$ h^{-1} for 2Ni@HZP-5-30, which were all much higher than those for 4Ni/HZ-5-80 (14.0 g[PA] $g[Ni]^{-1}$ h^{-1}). These results directly disclose that Ni@HZP-5 synthesized by the post-encapsulation could possess high hydrogenation and dehydration

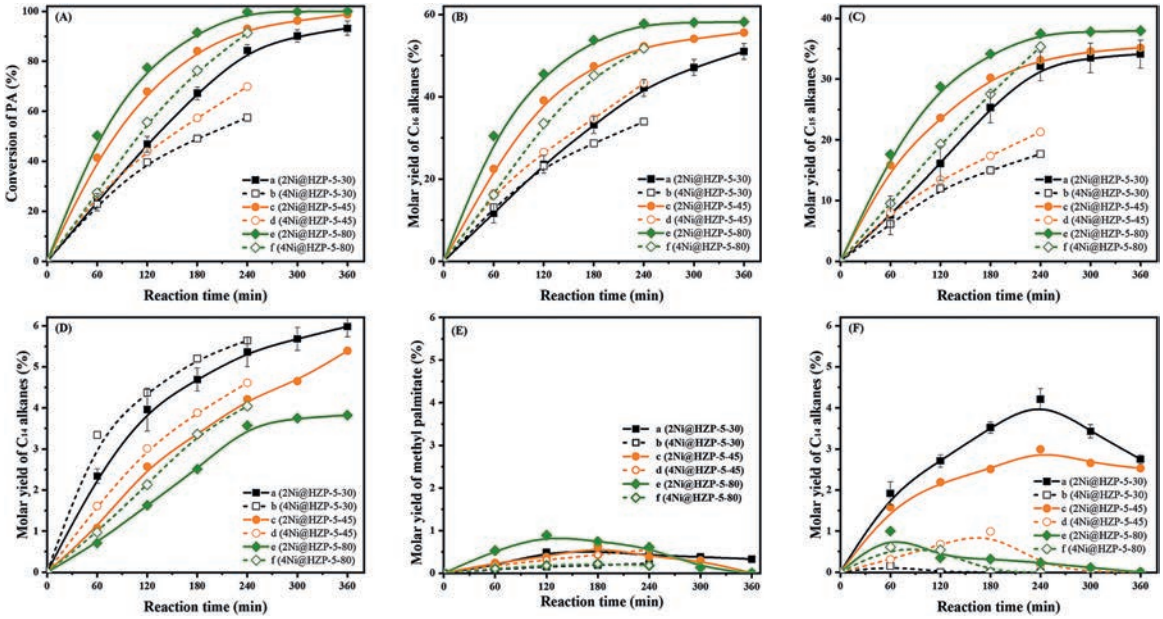

Fig. 2. Conversion of PA (A) and yield of products (B, C, D, E, F) over mNi@HZP-5-n (m = 2 or 4 wt% Ni, n = 30, 45 or 80 of Si/Al ratios) bi-functional catalysts with similar Ni contents (0.5 g PA in 50 mL n-decane; 0.2 g 2Ni@HZP-5-n and 0.1 g 4Ni@HZP-5-n; P = 4.0 MPa H_2; T = 260 °C; 800 rpm).

Table 1
Turn over frequency (TOF, g[PA] g[Ni]$^{-1}$ h^{-1}) of Ni@HZP-5 bi-functional catalysts compared to 4Ni/HZ-5-80 catalyst (0.5 g PA, 45 mL n-decane, 260 °C, 4.0 MPa H_2, 800 rpm).

Catalyst	Conversion (%)	TOF (g[PA] g[Ni]$^{-1}$ h^{-1})
4Ni/HZ-5-80 (0.25 g, 4.2 wt% Ni, 1 h)	29.5	14.0
4Ni@HZP-5-80 (0.1 g, 3.9 wt% Ni, 1 h)	26.4	33.8
2Ni@HZP-5-80 (0.2 g, 2.2 wt% Ni, 1 h)	59.3	67.4
4Ni@HZP-5-45 (0.1 g, 4.0 wt% Ni, 1 h)	25.7	32.1
2Ni@HZP-5-45 (0.2 g, 2.3 wt% Ni, 1 h)	41.4	45.0
4Ni@HZP-5-30 (0.1 g, 3.9 wt% Ni, 1 h)	22.9	29.4
2Ni@HZP-5-30 (0.2 g, 1.9 wt% Ni, 1 h)	24.0	31.6

activity, especially for high Si/Al ratios in spite of low Ni contents. The corresponding concentration of each component was shown in Table S2 (Supporting information).

The molar yields of main hydrocarbons over all Ni@HZP-5 are shown in Fig. 2B (C_{16} alkanes) and Fig. 2C (C_{15} alkanes). C_{16} and C_{15} alkanes were the dominant products *via* HDC and HDO routes in presence of H_2, and the increase yields of these two hydrocarbons were observed over Ni@HZP-5 with prolonging reaction time, like the various rules of PA conversion (Fig. 2A). Taking an example of 240 min, C_{16} and C_{15} alkanes were 57.7% and 37.5% for 2Ni@HZP-5-80, 52.3% and 33.1% for 2Ni@HZP-5-45, 42.2% and 33.5% for 2Ni@HZP-5-30, respectively. With complete conversion of PA, there was no obvious change of products' distribution over 2Ni@HZP-5-80 with prolonging reaction time to 300 min (58.1% C_{16} and 37.8% C_{15}) and 360 min (58.2% C_{16} and 37.9% C_{15}). Besides for C_{16} and C_{15} hydrocarbons, a few C_{12-14} alkanes were observed over all Ni@HZP-5 (Fig. 2D), which may be derived from the cracking of C_{15}/C_{16} alkanes [17,18]. With increasing the Si/Al ratios, C_{12-14} alkanes were 4.2% for 2Ni@HZP-5-30 (5.6% for 4Ni@HZP-5-30), 4.2% for 2Ni@HZP-5-45 (4.6% for 4Ni@HZP-5-45) and 3.6% for 2Ni@HZP-5-80 (4.0% for 4Ni@HZP-5-80) at 240 min. Slight isoalkanes (below 5%) were also obtained at 240 min during PA conversion despite of prolonging reaction time, which indicated that HZ-5 topology may do not favor isomerization compared to HMCM-49 [17,19] and/or HZSM-22 [20]. Trace yield of methyl palmitate was observed in Fig. 2E, which was formed *via* the esterification reaction between PA and 1-hexadecanol, and then was further cracked to C_{15} alkanes [5,17]. The slight hexadecanol was detected and could be quickly dehydrated to hydrocarbons, which suggested that dehydration reaction was not the determine step in this system.

Stability of 2Ni@HZP-5-80: During the deoxygenation process of fatty acids to diesel-like fuels, catalysts deactivation is considered as one of the biggest challenges, especially for impregnated catalysts with problems of metal leaching, migration, aggregation, sintering, *etc*. The stability of 2Ni@HZP-5-80 was importantly studied as shown in Figs. 3a and b. There were no obvious changes both for activity and hydrocarbons selectivity (Fig. 3a) over 2Ni@HZP-5-80 during 3 runs at identical conditions, which disclosed the outstanding stability. The hydrogenation activity and hydrocarbons selectivity over 2Ni@HZP-5-80 could recover completely after 3 runs and then regeneration (Fig. 3a-Reg.1). However, only 72.3% conversion of PA was obtained over impregnated 0.25 g 4Ni/HZ-5-80-Reg.1 with 50.2% C_{16} and 21.3% C_{15} alkanes in Fig. 3b, compared to fresh 4Ni/HZ-5-80 (75.5% conversion of PA, 49.5% C_{16} and 34.9% C_{15} alkanes), which indicated that there was some irreversible deactivation over 4Ni/HZ-5-80. Furthermore, 99.8% conversion of PA and 99.1% selectivity of hydrocarbons were obtained over 0.2 g 2Ni@HZP-5-80-Reg.2 (after 3 runs and 2 regenerations), basically the identical results over 0.2 g fresh 2Ni@HZP-5-80 (99.7% conversion of PA and 99.2% selectivity of hydrocarbons). This result confirmed the excellent stability of 2Ni@HZP-5-80 again, which point out the advantage of this post-encapsulation method. TEM analysis of 2Ni@HZP-5-80-Reg.2 was performed in Figs. 3c and d to show the superior stability of Ni nanoparticles about 3–7 nm, as well as the crystallinity of regeneration catalyst by XRD results in Fig. S6 (Supporting information). Additionally, the consecutively lattice fringe of ZSM-5 were observed without interrupted of the Ni nanoparticles both in 2Ni@HZP-5-45 (Fig. 1h) and 2Ni@HZP-5-80-Reg.2 (Fig. 3c), which directly indicated that Ni nanoparticles were encapsulated within ZSM-5 crystals not distributed in the outer surfaces. It is totally different from 4Ni/HZ-5-80-Reg.1 with obvious increase of Ni particles (Fig. S5-b) *via* the impregnation method.

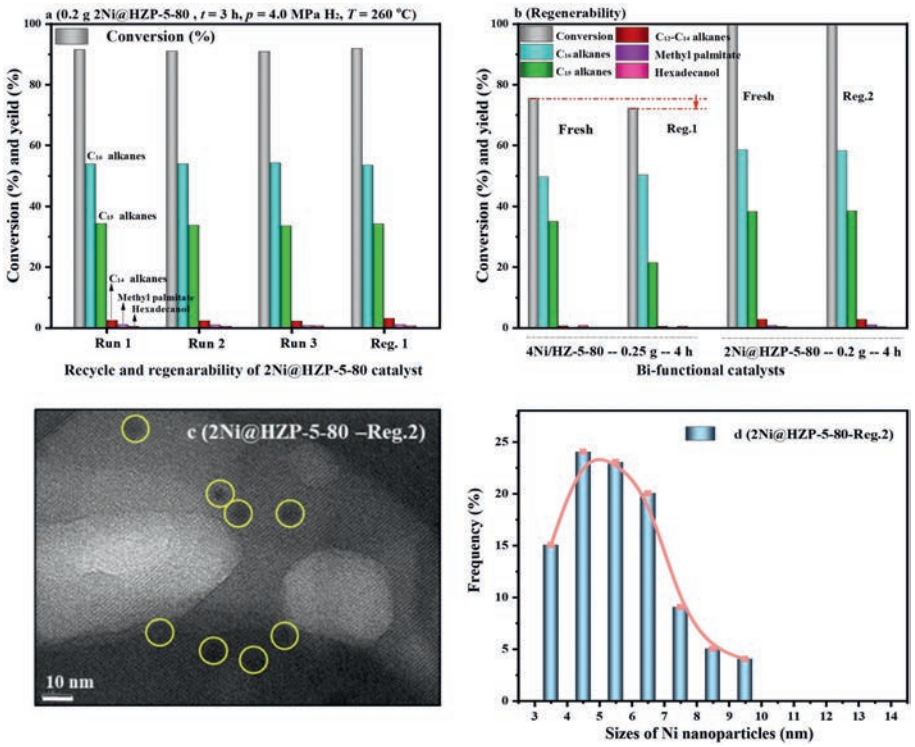

Fig. 3. (a, b) Stability of 2Ni@HZP-5-80 bi-functional catalysts and (c, d) TEM analysis of Reg.2 catalyst (0.5 g palmitic acid in 50 mL *n*-decane; $P = 4.0$ MPa H_2; $T = 260$ °C; 800 rpm).

According to above study, Ni encapsulation, Al addition and pores expansion were successfully achieved to synthesize meso-Ni@HZSM-5 bi-functional catalysts. About 3–7 nm Ni nano-particles were uniformly confined within HZSM-5 crystals. The less Ni contents and the higher Si/Al ratios led to the weaker interaction between Ni and Al, which was beneficial for the improvement of hydrogenation and acid-catalysis activities. All Ni@HZSM-5 *via* the post-encapsulation method exhibited more superior palmitic acid deoxygenation activity and yielded higher hydrocarbons selectivity than Ni/HZSM-5 *via* the impregnation method. Especially Ni@HZSM-5 (2 wt% Ni, Si/Al = 80) showed the highest conversion capacity of 67.4 g[PA] g[Ni]$^{-1}$ h^{-1}. Significantly, the outstanding stability of Ni@HZSM-5 were achieved during recycles and regeneration processes. There was no obvious deactivation for Ni@HZSM-5 after 3 runs and 2 regenerations, which was contributed to the excellent stability of Ni nano-particles *via* the post-encapsulation method. Therefore, the post-encapsulation of Ni within acid zeolites would offer a novel strategy to synthesize metal@zeolite bi-functional catalysts, which would effectively catalyze fatty acids to hydrocarbons.

Declaration of competing interest

The authors declare that they have no known competing financial interests or personal relationships that could have appeared to influence the work reported in this paper.

Acknowledgments

The authors are grateful for the financial supports from the Natural Science Foundation of China (No. 21908225) and the National Key Research and Development Program (No. 2018YFC1801501).

Appendix A. Supplementary data

Supplementary material associated with this article can be found, in the online version, at doi:10.1016/j.cclet.2021.06.086.

References

[1] W.B. Gong, C. Chen, H.J. Wang, et al., Chin. Chem. Lett. 29 (2018) 1617–1620.
[2] Y.D. Chen, F.Y. Liu, N.Q. Ren, S.H. Ho, Chin. Chem. Lett. 31 (2020) 2591–2602.
[3] S.Q. Xie, C.H. Jia, A. Prakash, et al., ACS Catal. 9 (2019) 3753–3763.
[4] J.A. Botas, D.P. Serrano, A. García, R. Ramos, Appl. Catal. B: Environ. 145 (2014) 205–215.
[5] M. Peroni, I. Lee, X.Y. Huang, et al., ACS Catal. 7 (2017) 6331–6341.
[6] W.H. Luo, W.X. Cao, P.C.A. Bruijnincx, et al., Green Chem. 21 (2019) 3744–3768.
[7] B. Ma, C. Zhao, Green Chem. 17 (2015) 1692–1701.
[8] J.M. Zhang, F.P. Tian, J.W. Chen, et al., Front. Chem. Sci. Eng. 15 (2020) 288–298.
[9] S.M. Wu, X.Y. Yang, C. Janiak, Angew. Chem. 131 (2019) 12468–12482.
[10] L. Liu, U. Díaz, R. Arenal, et al., Nat. Mater. 16 (2017) 132–138.
[11] J. Zhang, L. Wang, Y. Shao, Y.Q. Wang, B.C. Gates, Angew. Chem. Int. Ed. 56 (2017) 1–6.
[12] C.D. Wagner, W.M. Riggs, L.E. Davis, J.F. Moulder, G.E. Muilenberg, Handbook of X-ray Photoelectron Spectroscopy, 1979, p. 80.
[13] M. Zahmakiran, T. Ayvali, S. Akbayrak, et al., Catal. Today 170 (2011) 76–84.
[14] A. Fukuoko, N. Higashimoto, Y. Sakamoto, et al., Top. Catal. 18 (2002) 73–78.
[15] A. Mekki, A. Mokhtar, M. Hachemaoui, et al., Micropor. Mesopor. Mater. 310 (2021) 110597.
[16] Z. Jin, Y.F. Liu, L. Wang, et al., ACS Catal. 11 (2021) 1946–1951.
[17] Y.C. Shi, R. Li, Q.R. Shen, M.D. Yang, Y.L. Wu, Chem. Commun. 55 (2019) 12096–12099.
[18] X. Liu, M. Yang, Z.H. Deng, A. Dasgupta, Y. Guo, Chem. Eng. J. 20 (2020) 126332.
[19] Y.C. Shi, J.M. Zhang, E.H. Xing, Y.B. Xie, H.B. Cao, Ind. Eng. Chem. Res. 58 (2019) 21341–21349.
[20] Y.C. Shi, Y.Y. Cao, Y.N. Duan, et al., Green Chem. 18 (2016) 4633–4648.